

Large-eddy simulation of passive shock-wave/boundary-layer interaction control

Vito Pasquariello ^{*}, Muzio Grilli, Stefan Hickel, Nikolaus A. Adams

Lehrstuhl für Aerodynamik und Strömungsmechanik, Technische Universität München, D-85748 Garching, Germany

ARTICLE INFO

Article history:

Available online xxxx

Keywords:

LES
Compressible flow
Low-frequency unsteadiness
SWBLI

ABSTRACT

We investigate a passive flow-control technique for the interaction of an oblique shock generated by an 8.8° wedge with a turbulent boundary-layer at a free-stream Mach number of $Ma_{\infty} = 2.3$ and a Reynolds number based on the incoming boundary-layer thickness of $Re_{\delta_0} = 60.5 \times 10^3$ by means of large-eddy simulation (LES). The compressible Navier-Stokes equations in conservative form are solved using the adaptive local deconvolution method (ALDM) for physically consistent subgrid scale modeling. Emphasis is placed on the correct description of turbulent inflow boundary conditions, which do not artificially force low-frequency periodic motion of the reflected shock. The control configuration combines suction inside the separation zone and blowing upstream of the interaction region by a pressure feedback through a duct embedded in the wall. We vary the suction location within the recirculation zone while the injection position is kept constant. Suction reduces the size of the separation zone with strongest effect when applied in the rear part of the separation bubble. The analysis of wall-pressure spectra reveals that all control configurations shift the high-energy low-frequency range to higher frequencies, while the energy level is significantly reduced only if suction acts in the rear part of the separated zone. In that case also turbulence production within the interaction region is significantly reduced as a consequence of mitigated reflected shock dynamics and near-wall flow acceleration.

© 2014 Published by Elsevier Inc.

1. Introduction

Shock-wave/boundary-layer interactions (SWBLI) frequently occur in flows of technological interest, such as supersonic air intakes, turbomachine cascades, helicopter blades, supersonic nozzles and launch vehicles in general. SWBLI can critically affect the vehicle or machine performance in several ways. The adverse pressure gradient acting on the flow strongly retards the boundary-layer, eventually leading to separation if the imposed pressure gradient is strong enough (Dély and Dussauge, 2009).

A schematic of the basic interaction type studied in this work is shown in Fig. 1. The adverse pressure gradient imposed by the incident shock C_1 is large enough to cause separation of the boundary-layer. Separation takes place well ahead of the inviscid impingement x_{imp} . The upstream propagation of the pressure gradient within the subsonic part of the turbulent boundary-layer (TBL) induces compression waves in the supersonic part of the TBL, which coalesce to the reflected shock C_2 . The reflected shock intersects the incident shock at point I and the original shocks continue traveling as the transmitted shocks C_3 and C_4 , respectively. The

shock C_4 penetrates into the separated shear layer, curves due to the local Mach number variation and finally reflects at the sonic line as an expansion fan. Pirozzoli and Grasso (2006) found from their direct numerical simulation (DNS) of an impinging shock on a $Ma = 2.25$ TBL that the formation of the detached shear layer is primarily responsible for turbulence amplification. The separated shear layer follows the inclination of the initial part of the separation bubble, while being deflected towards the wall due to the expansion fan and finally reattaching further downstream. The compression waves associated with reattachment merge to form the reattachment shock C_5 . Downstream of the SWBLI the TBL recovers an equilibrium state.

Until the 1950s SWBLI have been described as a steady process, which nowadays is known to be incorrect when shock-induced separation occurs. As stated by Dolling (2001), the interaction region is the main source of maximum mean and fluctuating pressure levels as well as thermal loads. Turbulence production is enhanced in the vicinity of the mean separation location which in turn increases viscous dissipation in this region (Dély and Dussauge, 2009). The low-frequency unsteadiness of the reflected shock is a crucial aspect with regard to the choice of materials concerning supersonic engine-inlets, since it is a main contribution to failure due to fatigue (Pirozzoli et al., 2010).

* Corresponding author. Tel.: +49 89 289 16121.

E-mail address: vito.pasquariello@tum.de (V. Pasquariello).

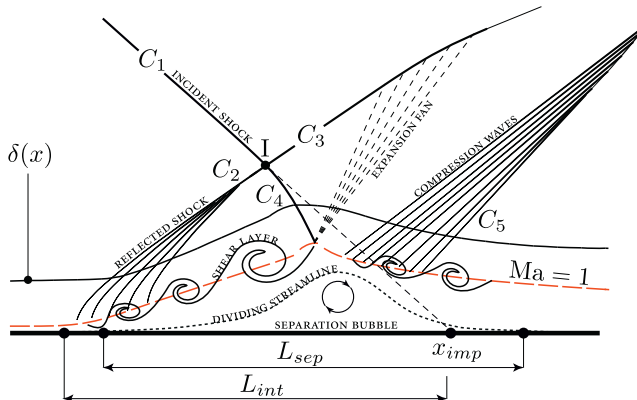


Fig. 1. Schematic of the oblique shock/boundary-layer interaction with mean separation.

Several experiments Dolling and Bogdonoff (1981), Beresh et al. (2002), Dupont et al. (2006), Ganapathisubramani et al. (2007) and numerical investigations by means of direct numerical simulations Adams (2000), Pirozzoli and Grasso (2006), Wu and Martín (2007), Priebe and Martín (2012) and large-eddy simulations Loginov et al. (2006), Touber and Sandham (2009b), Pirozzoli et al. (2010), Grilli et al. (2012, 2013) unanimously confirmed the existence of such low-frequency motions, which typically reveal themselves by a “breathing” motion of the separation bubble, accompanied by an oscillatory movement of the reflected shock. The nomenclature “low-frequency” emphasizes the fact that the characteristic frequency of the incoming TBL is approximately two or three orders of magnitude higher than the one related to the shock unsteadiness. Touber and Sandham (2011) have shown that the separation acts as a broadband amplifier, imposing additional problems for vehicles with SWBLI since upstream disturbances get amplified through the shock system which in turn probably decrease the vehicle's performance.

On this account research is motivated with the goal to identify suitable control mechanisms that reduce pressure and heat loads due to unsteady SWBLI, see Dély (1985). One can distinguish between *boundary-layer control* mechanisms, which aim at reducing shock-induced separation, and *shock control* mechanisms, which reduce stagnation pressure losses. Dély (1985) and Viswanath (1988) report a great number of suitable boundary-layer control methods such as tangential blowing upstream of the interaction region, suction within the separation bubble, wall-cooling and vortex generators. These techniques all have in common that they reduce the separation length by additionally supplying momentum to the near-wall flow, hence making the incoming TBL less susceptible against an adverse pressure gradient. Souverein and Debièvre (2010) investigated the influence of Air Jet Vortex Generators (AJVGs) placed in a row upstream of the interaction region for an impinging SWBLI at $M = 2.3$ and 9.5° deflection angle, consistent with the flow conditions at IUSTI (“Institution Universitaire des Systèmes Thermiques Industriels, Marseille”, Doerffer et al. (2011)), and reported a significant reduction of the recirculation zone both in length and height due to the enhanced mixing process initiated through the generation of counter-rotating vortices. Moreover, the characteristic frequency associated with the reflected shock increases by about 50%, which is an important finding concerning practical control applications. Experimental studies McCormick (1993) and Blinde (2008) and numerical simulations Lee (2009) and Ghosh (2010) for the control technique involving structural vortex generators both revealed a significant reduction of the shock-induced separation, accompanied by an improvement of the boundary-layer characteristics

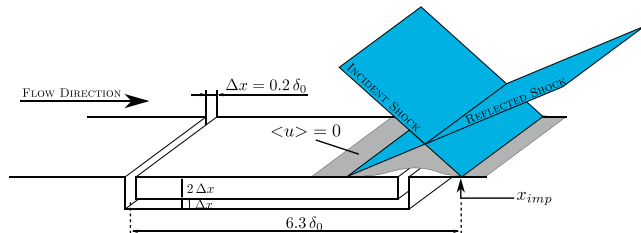


Fig. 2. Schematic of the considered control method. Blue planes: reflected shock system. Grey Surface: 2D sketch of the recirculation region. (For interpretation of the references to color in this figure legend, the reader is referred to the web version of this article.)

downstream of the interaction region. A recent numerical study performed by Bisek et al. (2012) for a control strategy resembling a magnetically-driven gliding-arc discharge model has shown, that besides a substantial reduction of separation length up to 75%, the low-frequency content from wall-pressure spectra can be removed.

The current work is motivated by the control configurations reported by McCormick (1993) and Fulker (1999), where a pressure feedback is generated downstream and upstream of the shock impingement region. For this purpose a porous surface with a common plenum beneath it was placed in the region of the shock impingement. A natural recirculating flow is generated, bleeding boundary layer flow from the high-pressure to the low-pressure side. In order to have better control on the effect of the precise location of suction and blowing, we replace the porous surface and cavity by a duct, see Fig. 2. The duct spans the entire spanwise domain extent, which leads to a quasi two-dimensional control configuration. The main objective of this paper is to evaluate the influence of the applied control technique on mean flow properties, turbulence structure within the interaction region and unsteady shock dynamics by analysing results from implicit large-eddy simulations. Details of the flow configuration are given in Section 2 and the underlying numerical approach is described in Section 3. Numerical results are presented and analysed in Section 4. Conclusions are drawn in Section 5.

2. Flow configuration

The basic SWBLI topology studied in this work is the case of an oblique shock impinging on a flat plate boundary-layer. The resulting flow pattern is shown in Fig. 3. The shock is generated by a 8.8° wedge at a freestream Mach number of $Ma_\infty = 2.3$ and the Reynolds number based on the inlet boundary-layer thickness is $Re_{\delta_0} = 60.5 \times 10^3$. Stagnation temperature and pressure are $T_0 = 300\text{ K}$ and $p_0 = 0.5\text{ bar}$. Table 1 summarizes the flow

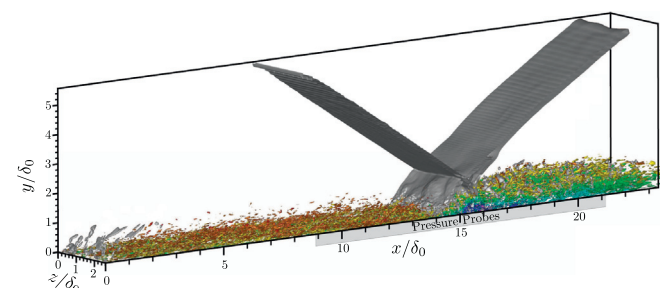


Fig. 3. Illustration of the computational domain together with isocontours of pressure gradient magnitude (gray) and Q-criterion (colored by local streamwise velocity). (For interpretation of the references to color in this figure legend, the reader is referred to the web version of this article.)

Table 1

Flow parameters.

Flow parameters	
M_∞	2.3
Θ	8.8°
T_0	300 (K)
p_0	0.5 (bar)
Re_{δ_0}	60524
δ_0 ^a	11.35 (mm)
δ_0^r ^b	13.46 (mm)

^a Evaluated at the domain inlet.^b Evaluated at a reference plane at $x/\delta_0 = 11.7$.

conditions. Throughout this study we will use the boundary-layer thickness either evaluated at the domain inlet $\delta_0 = 11.35$ mm or at a reference plane $\delta_0^r = 13.46$ mm located upstream of the interaction region at $x/\delta_0 = 11.7$ as reference length. The boundary-layer thickness is calculated based on the distance from the wall where 99% of the mean free-stream velocity U_∞ is reached.

The computational domain is rectangular with dimensions $23.39\delta_0 \times 5.57\delta_0 \times 2.62\delta_0$ and is discretized with $560 \times 190 \times 130$ cells in streamwise, wall-normal and spanwise directions, respectively. This leads to a grid resolution of $\Delta x^+ = 30$, $\Delta y_{min}^+ = 1.2$, $\Delta z^+ = 15$ at the reference plane. In the wall-normal direction hyperbolic grid stretching is used with a stretching factor of $\beta_y = 5.0$

$$y(j) = L_y \cdot \frac{\sinh\left(\frac{\beta_y(j-1)}{N_y-1}\right)}{\sinh(\beta_y)}, \quad (1)$$

where j denotes the individual grid point, L_y the domain height and N_y the total number of cells in wall-normal direction.

For the low-frequency analysis presented later, 10,387 equally spaced pressure probes ($\Delta/\delta_0^r \approx 0.05$) have been placed both in stream- and spanwise direction along the wall within the region indicated in Fig. 3.

Fig. 2 shows a schematic of the basic control method used in this work together with the main geometry parameters. In total three parameter sets have been investigated, for which the suction location within the separated zone is varied while the injection position is kept fix. Intuitively, vertical injection perturbs the incoming TBL, followed by a relaxation process before the interaction region is reached. For this reason the injection is located well upstream of the nominal inviscid impingement point. Fig. 4 shows the average normalized wall-pressure distribution for the baseline configuration without control, referred to as NC in the following, together with the bubble topology represented through the

Table 2

Numerical details of all cases studied.

Case	NC	CA	CB	CC
<i>Statistics acquisition</i>				
Runtim ^a TU_∞/δ_0^r	1113	945	929	1004
Timestep $\Delta t U_\infty/\delta_0^r \cdot 10^{-3}$	1.5	0.9	0.9	0.9
Sampling rate ^b $\Delta t U_\infty/\delta_0^r$	0.01	0.01	0.01	0.01
Number of FIT	56	48	47	51
<i>LF-Analysis</i>				
Sampling rate ^c $\Delta t U_\infty/\delta_0^r$	0.045	0.026	0.026	0.026
$St_{min} = f_{min} \delta_0^r/U_\infty$	0.001	0.001	0.001	0.001
$St_{max} = f_{max} \delta_0^r/U_\infty$	11	19	19	19

^a Excluding a start-up transient of 5 FITT.^b Sampling time for the post-processing based on collected snapshots.^c Mean sampling time for the wall-pressure probes.

$\langle u \rangle/U_\infty = 0$ iso-line (●). Grey shaded rectangles represent three different suction locations under investigation. With CA we denote the case where suction is applied near the maximum bubble height and for the cases CB and CC the suction slot is shifted 0.3 δ_0 upstream and downstream, respectively.

3. Numerical approach

We solve the three-dimensional compressible Navier–Stokes equations in conservative form

$$\partial_t \mathbf{U} + \nabla \cdot \mathbf{F}(\mathbf{U}) + \nabla \cdot \mathbf{D}(\mathbf{U}) = 0, \quad (2)$$

with the state vector $\mathbf{U} = [\rho, \rho u_1, \rho u_2, \rho u_3, E]$ consisting of: density ρ , momentum ρu_i and total energy E . In the above equation the total flux is split into an inviscid part

$$\mathbf{F}_i(\mathbf{U}) = [u_i \rho, u_i \rho u_1 + \delta_{i1} p, u_i \rho u_2 + \delta_{i2} p, u_i \rho u_3 + \delta_{i3} p, u_i(E + p)], \quad (3)$$

and a viscous contribution

$$\mathbf{D}_i(\mathbf{U}) = [0, -\tau_{i1}, -\tau_{i2}, -\tau_{i3}, u_k \tau_{ik} + q_i], \quad (4)$$

where u_i is the velocity vector and τ_{ij} the viscous stress tensor, which according to the Stokes hypothesis for a Newtonian fluid is

$$\tau_{ij} = \mu(T)(\partial_j u_i + \partial_i u_j - 2/3 \delta_{ij} \partial_k u_k). \quad (5)$$

The heat fluxes q_i due to conduction follow from the Fourier law

$$q_i = -\kappa(T) \partial_i T. \quad (6)$$

The above equations are solved in non-dimensional form where the normalization process reads

$$\begin{aligned} u_i &= u_i^*/U_\infty^*, \quad \rho = \rho^*/\rho_\infty^*, \quad T = T^*/T_\infty^*, \quad p \\ &= p^*/(\rho_\infty^* U_\infty^{*2}), \quad E = E^*/(\rho_\infty^* U_\infty^{*2}), \quad x_i = x_i^*/\delta^*, \quad t \\ &= t^* U_\infty^*/\delta^*, \end{aligned} \quad (7)$$

and variables marked with a star (★) represent dimensional quantities. The governing flow parameters are the Reynolds number Re , the Prandtl number Pr , the Mach number Ma and the specific-heat ratio γ . We consider a perfect gas with a constant Prandtl number of $Pr = 0.72$ and specific-heat ratio of $\gamma = 1.4$. Pressure p and temperature T are determined by the non-dimensional ideal-gas equation of state

$$p = \frac{1}{\gamma Ma^2} \rho T, \quad (8)$$

and the definition of total energy E

$$E = \frac{p}{\gamma - 1} + \frac{1}{2} \rho u_i u_i. \quad (9)$$

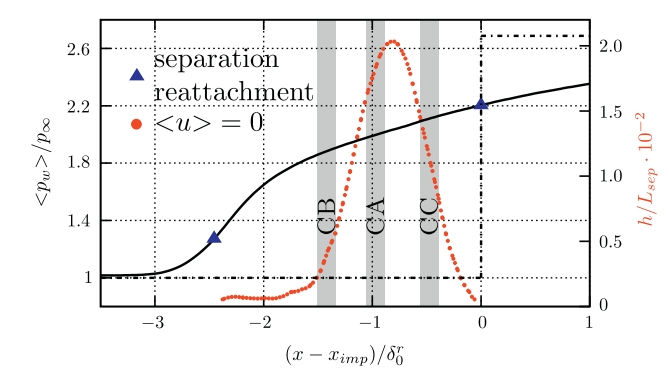


Fig. 4. Average normalized wall-pressure distribution and zero streamwise velocity iso-line for the uncontrolled reference configuration NC. Investigated suction locations are indicated by CA, CB and CC. Triangles (▲) denote separation and reattachment pressure levels, respectively.

Temperature dependence of dynamic viscosity $\mu(T)$ and thermal conductivity $\kappa(T)$ are modeled through the Sutherland law

$$\mu(T) = \frac{1}{Re} T^{1.5} \frac{1+C}{T+C} \quad \text{with} \quad C = \frac{S}{T_\infty^*}, \quad S = 110.4 \text{K}$$

$$\kappa(T) = \frac{1}{(\gamma-1)\text{Ma}^2\text{Pr}} \mu(T). \quad (10)$$

The compressible Navier-Stokes equations are solved using the Adaptive Local Deconvolution Method (ALDM) for the discretization of the convective fluxes Hicken et al. (2006) and Hicken and Larsson (2009). ALDM is a nonlinear finite volume method that provides a physically consistent subgrid-scale turbulence model for implicit LES. Employing a shock sensor to detect discontinuities and switch on the shock-dissipation mechanism, ALDM can capture shock waves while smooth waves and turbulence are propagated accurately without excessive numerical dissipation. The diffusive fluxes are discretized using a 2nd order central difference scheme, and a 3rd order Runge Kutta scheme is used for the time integration.

At the domain inlet a Digital Filter (DF) based boundary condition is used (Toubal and Sandham, 2009b), for which first and second order statistical moments have been obtained through a precursor temporal boundary-layer simulation under the same flow conditions. The shock is introduced at the top of the domain by imposing a jump in the flow variables that satisfies the Rankine-Hugoniot relations. The nominal inviscid impingement point at the wall is $x_{imp} = 16.7\delta_0$. At the outlet, linear extrapolation of all flow variables is used. The wall is modeled as isothermal with the temperature fixed to its nominal adiabatic value $T_w/T_\infty = 1 + r^{\frac{j-1}{2}} M_\infty^2 = 2.065$, which corresponds to a recovery factor of $r = 1$. Periodic boundary conditions are used in the spanwise direction. Statistical quantities have been obtained by averaging instantaneous three-dimensional flow fields in time and spanwise direction after an initial transient of $5L_x/U_\infty$; see Table 2 for details. In the following Reynolds averages will be denoted as $\langle \dots \rangle / \dots$ and Favre averages as $\overline{\dots}$.

4. Results and discussion

4.1. Incoming turbulent boundary-layer

According to Grilli et al. (2013), the spatial extent of the separation bubble in SWBLI is highly sensitive on the level of turbulence in the incoming TBL. Thus, before the influence of each control configuration on the SWBLI is addressed, the main incoming boundary-layer properties will be discussed. The van-Driest transformed mean-velocity profile together with the RMS of Reynolds stresses in Morkovin scaling at $x/\delta_0 = 13.1$ are presented in Fig. 5(a)/(b) and compared with DNS data of Pirozzoli and Bernardini (2011) for identical friction Reynolds number $Re_\tau = 900$. Note that the DNS has a slightly different Mach number of $\text{Ma}_\infty = 2.0$ ($\text{Ma}_{\infty,\text{LES}} = 2.3$) and a lower local Reynolds number of $Re_\delta = 55,170$ ($Re_{\delta,\text{LES}} = 73,756$). The velocity profile is in good agreement with the logarithmic law of the wall and the DNS data, with small differences in the wake region due to higher Reynolds number. The Reynolds stresses are in good agreement with the DNS data in the near-wall region, while larger deviations occur in the logarithmic and wake region.

For further validation, the incompressible skin friction distribution $\langle C_f \rangle$, obtained from the van-Driest II transformation (van Driest, 1956), is compared to algebraic incompressible relations, various DNS and experimental data for a wide range of Mach numbers; see Fig. 6(a). Reported incompressible skin friction formulas by Kármán-Schoenherr and Blasius are adopted from Hopkins and Inouye (1971) and the relation by Smits is adopted from

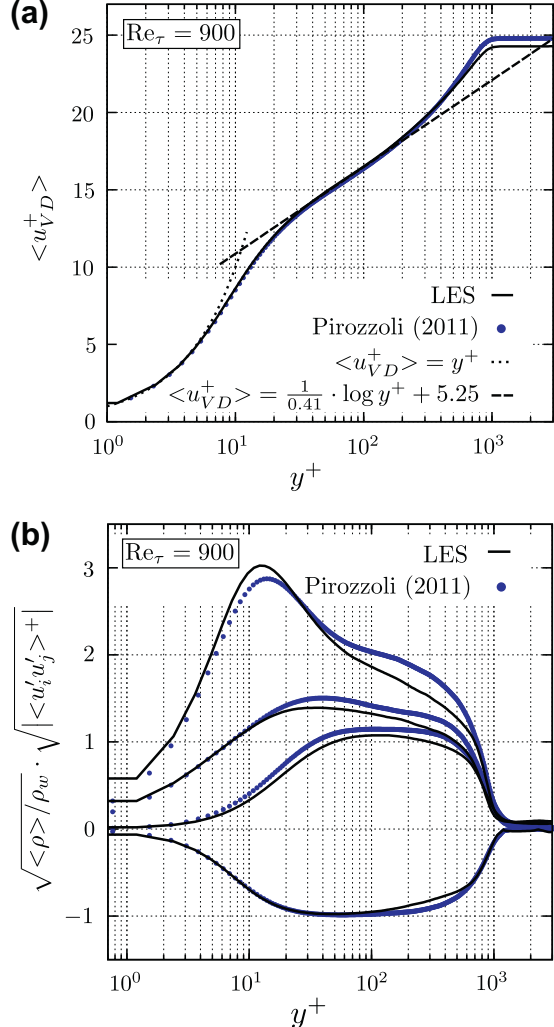


Fig. 5. Incoming boundary-layer: (a) van-Driest transformed mean-velocity profile. (b) RMS of Reynolds stresses with density scaling at $Re_\tau = 900$.

Smits et al. (1983). The computed incompressible skin friction coefficient (—) is in good agreement with the reported empirical relations. Autocorrelation functions in spanwise direction, evaluated at the streamwise position $x/\delta_0 = 11.7$ and wall-normal distance $y/\delta_0 = 0.1$, are reported in Fig. 6(b). The figure shows that all flow variables are sufficiently decorrelated over a distance equal to half of the spanwise domain extent. We conclude that the domain is sufficiently large and that the turbulence structure is not affected by the periodic boundary conditions. In the same figure, also the streamwise evolution of the autocorrelation functions for $y/\delta_0 = 0.1$ is illustrated. It is important to note, that the DF inflow technique does not introduce any spurious low-frequency forcing and does not interfere with the reflected shock dynamics investigated in this study.

Finally, Fig. 7 reports the turbulence kinetic energy (TKE) budgets together with the anisotropy invariant map (AIM) evaluated at the reference station $x/\delta_0 = 11.7$. The transport equation for the mean TKE $k = 1/2 u''_i u''_j$ for a compressible flow can be written as

$$\frac{\partial \bar{p}k}{\partial t} = C + T + P + D + \Pi - \varepsilon + M = 0, \quad (11)$$

where the single budgets on the right hand side are the contributions due to convection C ($-\partial_{x_j} [\bar{\rho} \bar{u}_j k]$), turbulent transport T

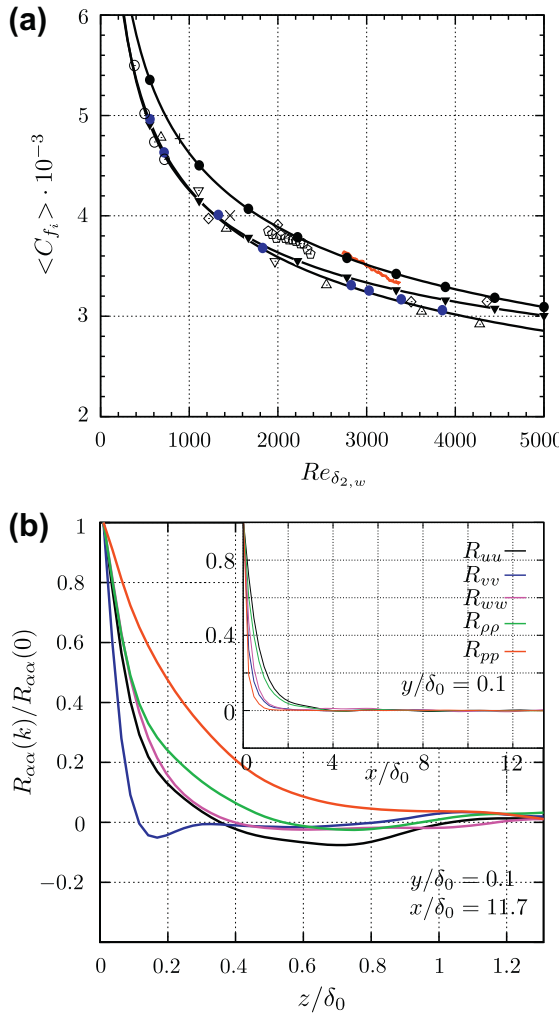


Fig. 6. Incoming boundary-layer: (a) Incompressible skin friction evolution. (—•—) Blasius; (—▼—) Kármán-Schoenherr; (—□—) Smits; (———) Present LES; (○) Pirozzoli and Grasso (2004), (●) Pirozzoli and Bernardini (2011), (○) Komminaho and Skote (2002), △ Schlatter and Örlü (2010), (▽) Simens et al. (2009), (◊) CAT5301 AGARD 223, (+) Guarini et al. (2000), (×) Maeder et al. (2001). (b) Two-point autocorrelation functions.

$(-\partial_{x_j}[1/2\bar{\rho}u_i'\bar{u}_i''\bar{u}_j' + \bar{p}'\bar{u}_i'\delta_{ij}])$, production $P(-\bar{\rho}\bar{u}_i'\bar{u}_j''\partial_{x_j}\bar{u}_i)$, viscous diffusion $D(\partial_{x_j}[\bar{u}_j'\bar{u}_i''])$, pressure-dilatation $\Pi(\bar{p}'\partial_{x_i}\bar{u}_i'')$, viscous dissipation $\epsilon(\bar{\tau}_{ij}'\partial_{x_j}\bar{u}_i'')$ and compressible mass flux $M(\bar{u}_i''[\partial_{x_j}\bar{\tau}_{ij} - \partial_{x_i}\bar{p}])$. For a detailed discussion of the single terms refer to e.g. Shahab et al. (2011). Consistent with observations for a canonical boundary-layer flow, production and dissipation are balanced over a large part of the boundary-layer starting from $y^+ > 40$ in the logarithmic layer (Pope, 2000). In the viscous sublayer ($y^+ < 5$) the main contributions are due to viscous diffusion, transporting kinetic energy all the way to the wall, and viscous dissipation, whereas contributions due to convection are negligible small. The production peak is observed within the buffer layer at $y^+ = 10$, where the excess energy produced cannot be balanced by viscous dissipation, but is transported away by turbulent transport.

Following the work of Lumley (1978), the second II_b and third III_b invariant of the anisotropic Reynolds stress tensor $b_{ij} = \bar{u}_i'\bar{u}_j''/2k - 1/3\delta_{ij}$ provide a representative description of the turbulent state. Each vertex in the (III_b, II_b) map, also known as the "Lumley triangle", constitutes a special turbulence state, see Fig. 7(b) for details. A two-component turbulence state is found for the near-wall flow, with highest anisotropy in the buffer layer.

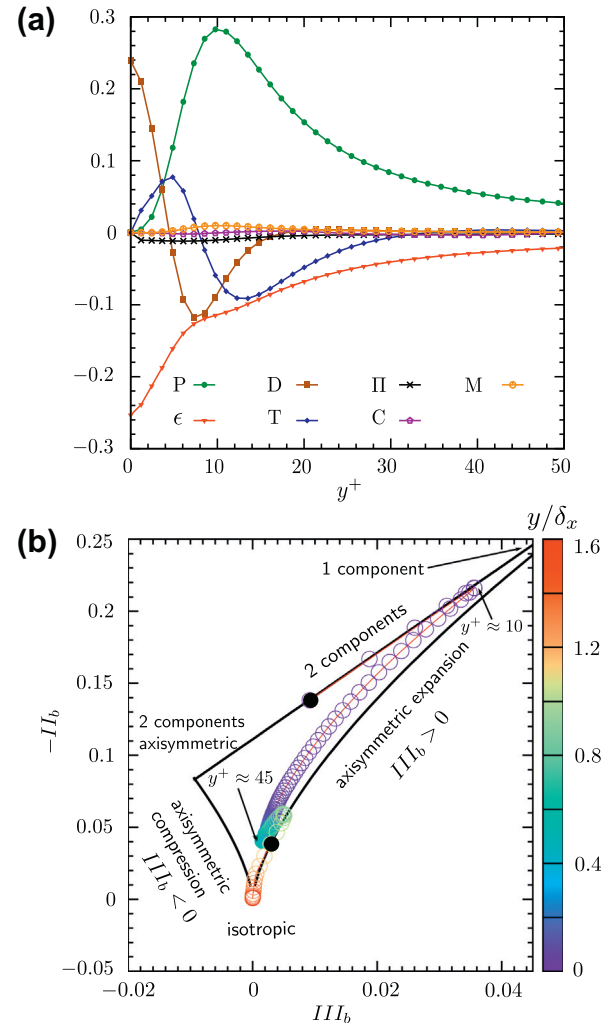


Fig. 7. (a) Turbulent kinetic energy transport equation evaluated at $x/\delta_0 = 11.7$. Individual budgets are normalized by $\rho_w u_w^4/v_w$. (b) Reynolds stress anisotropy invariant map evaluated at $x/\delta_0 = 11.7$. Black bullets • represent the wall and boundary-layer edge locations, respectively. The wall-normal distance is represented through the colorbar and normalized by the local boundary-layer thickness δ_x . (For interpretation of the references to color in this figure legend, the reader is referred to the web version of this article.)

($y^+ \approx 10$). Within the buffer layer the path turns and follows the limit of axisymmetric expansion while gradually returning to an isotropic state in the outer layer.

4.2. Baseline SWBLI – NC

The mean skin-friction evolution in the direct vicinity of the interaction region is shown in Fig. 8(a). Due to the adverse pressure gradient imposed on the turbulent boundary-layer, the flow is decelerated and forms a recirculation zone as indicated by the change of sign in $\langle C_f \rangle$. The mean separation length for the baseline configuration is $L_{sep} = 2.46\delta_0$. The corresponding wall-pressure evolution is shown in Fig. 4. The pressure increase associated with the impinging shock is felt approximately $3\delta_0^r$ before the theoretical inviscid impingement location x_{imp} . This effect is known as the upstream influence mechanism (Délery, 1985). Black triangles denote the separation and reattachment pressure levels. The bubble topology, analyzed through the $\langle u \rangle/U_\infty = 0$ iso-line in Fig. 4, reveals a very shallow separation zone with an aspect ratio of $L_{sep}/h_{max} = 50$, consistent with numerical simulations performed

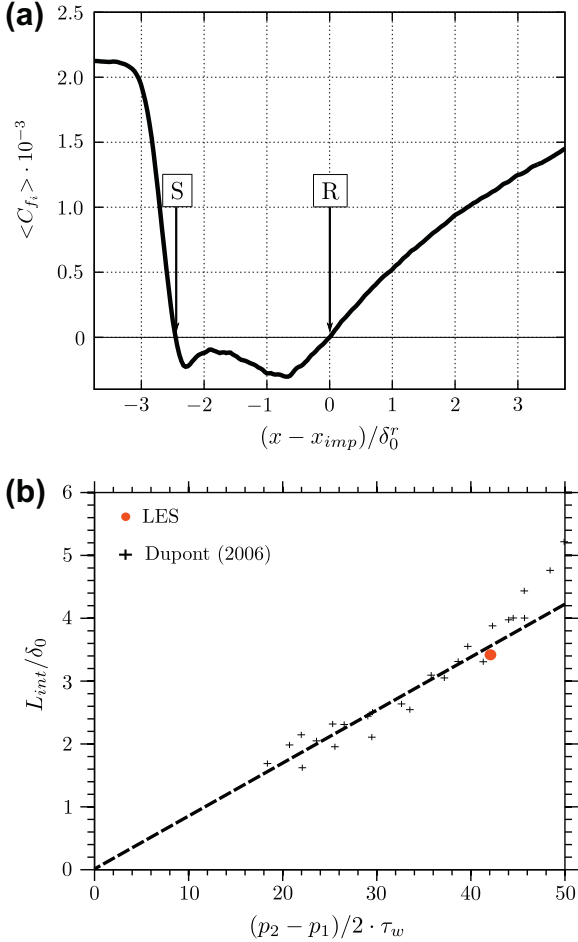


Fig. 8. Mean-flow statistics: skin friction evolution and interaction length.

by Touber and Sandham (2009a) for the IUSTI case. Dupont et al. (2006) proposed a linear relationship for weak interactions between the interaction length L_{int} and the pressure jump across the impinging shock wave $(p_2 - p_1)$ normalized by the upstream boundary-layer thickness δ_0 and wall shear stress τ_w , respectively. In this study we define the distance between the mean reflected shock foot position (obtained through linear extrapolation to the wall) and x_{imp} as the interaction length L_{int} , as done by Dupont et al. (2006). Fig. 8(b) shows the experimental data together with the value for the current LES (●), confirming the expected linear relationship.

In the following we analyze the Power Spectral Densities (PSD) of wall-pressure probes in order to address unsteady aspects related to reflected shock dynamics. Pressure signals have been recorded at a mean sampling time interval of $0.045\delta_0^r/U_\infty$ and cover a total timespan of $1113\delta_0^r/U_\infty$; see Table 2 for details. This leads to a maximum resolvable Strouhal number of $St_{max} \approx 11$ and a minimum resolvable Strouhal number of $St_{min} \approx 0.001$, which means that the current LES is well able to capture the expected low-frequency unsteadiness. In Fig. 9 we report the wall-pressure spectrum together with the full evolution of pressure fluctuations evaluated at four selected streamwise locations. Moreover, mean separation [S] and reattachment [R] positions are indicated. In order to emphasize the frequencies that contribute most, we show contours of the premultiplied PSD normalized by the integrated PSD over a given frequency range, i.e., $f \cdot PSD(f) / \int f \cdot PSD(f) df$. The spectra have been obtained with the Welch algorithm by splitting the time-signal in eight segments

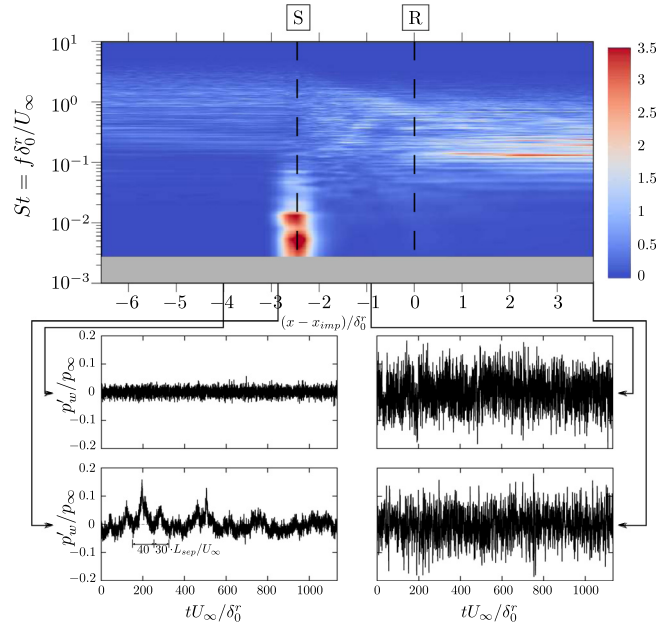


Fig. 9. Weighted power spectral density (PSD) of spanwise-averaged wall-pressure signals for the baseline configuration and selected pressure signals. Contour: $f \cdot PSD(f) / \int f \cdot PSD(f) df$.

with 50% overlap using Hamming windows. The most upstream wall-pressure variance signal shows no significant pressure variation, indicating the undisturbed turbulent boundary-layer. Considering the next probe, which is located in the proximity of the mean reflected shock foot, distinctive pressure peaks associated with the back and forth motion of the reflected shock can be identified. Dussauge et al. (2006) found typical Strouhal numbers based on the separation length ranging between $St_{Lsep} = 0.02, \dots, 0.05$ for different flow geometries and upstream conditions. Associated

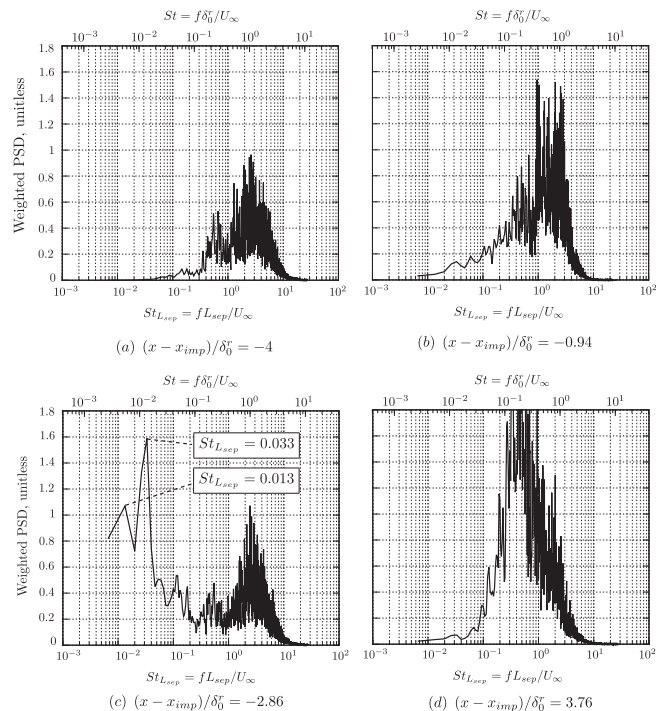


Fig. 10. Weighted power spectral density (PSD) associated to pressure variance signals reported in Fig. 9.

time scales of $tU_\infty/\delta_{sep} = 20, \dots, 50$ could be found in the current LES as indicated in Fig. 9. Further downstream, distinct peaks are no longer visible, however, the amplitude of the pressure fluctuations has increased significantly as a consequence of turbulence amplification over the shock. The PSD spectrum in Fig. 9 clearly shows the broadband peak associated with the characteristic frequency of the energetic scales in the undisturbed TBL, being U_∞/δ_0^r . The energy peak shifts towards significantly lower frequencies in the vicinity of the mean separation location and moves back again to higher frequencies downstream of the interaction zone. Due to the thickening of the boundary-layer past the shock system, the new PSD peak is located at lower Strouhal numbers. Fig. 10 reports weighted PSDs related to the wall-pressure signals shown in Fig. 9. It is important to note that no energetically significant low-frequencies have been introduced by the inflow technique used for the current LES, hence allowing to state that the SWBLI dynamics are not artificially influenced by upstream events. Based on the mean separation length a Strouhal number of $St_{sep} = fL_{sep}/U_\infty = 0.03$ is found for the low-frequency shock motion. This finding is consistent with experimental values documented in Dupont et al. (2006). Based on this characteristic frequency a total number of 15 low-frequency cycles (LFC) are captured within the available integration time.

4.3. Control configurations

In this section, we provide a cross-comparison between the uncontrolled baseline case NC and the three control configurations CA, CB and CC. A general impression of the effect of flow control is given in Figs. 11 and 12, where contour plots of the instantaneous and time-averaged temperature distribution within the $x-y$

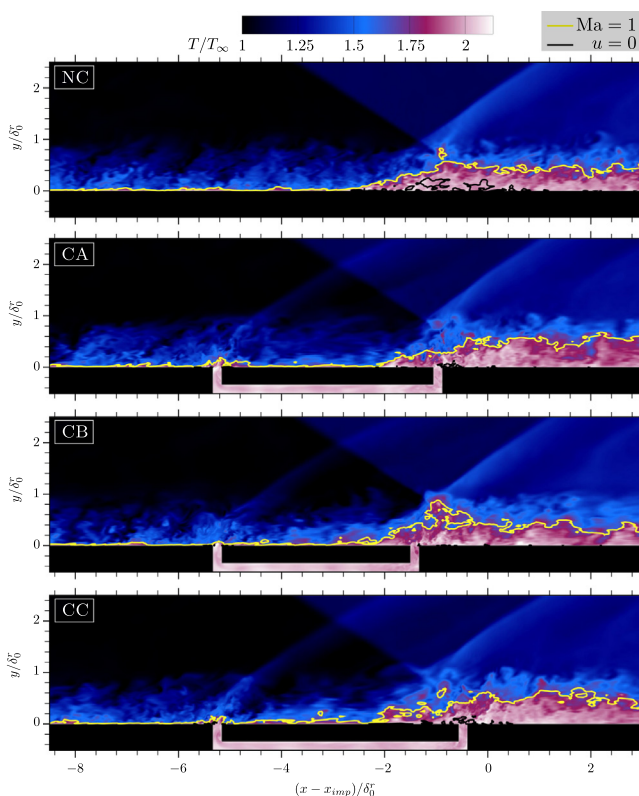


Fig. 11. Instantaneous temperature distribution T/T_∞ in $x-y$ mid-plane with $\text{Ma} = 1$ isoline in yellow and $u = 0$ isoline in black for all configurations studied. (For interpretation of the references to color in this figure legend, the reader is referred to the web version of this article.)

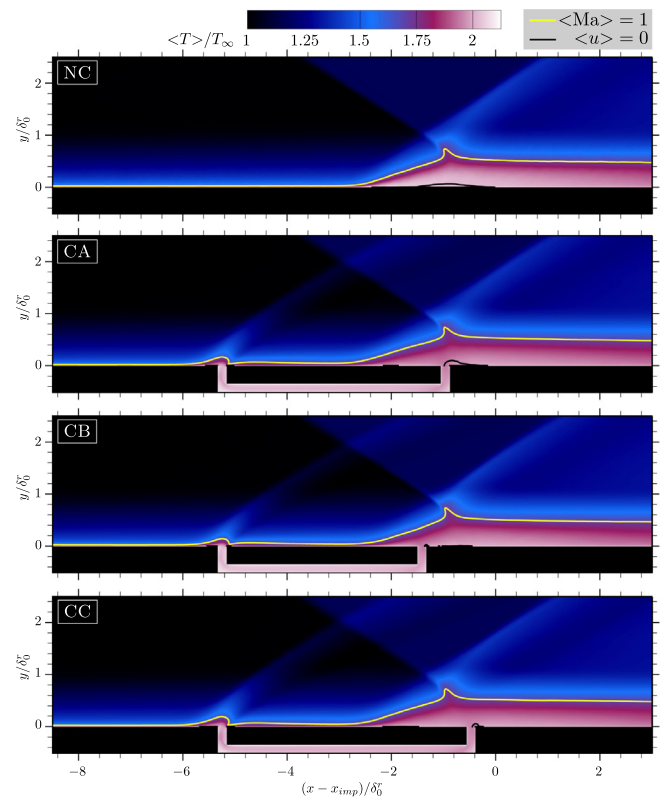


Fig. 12. Time-averaged temperature distribution $\langle T \rangle / T_\infty$ in $x-y$ mid-plane with $\langle \text{Ma} \rangle = 1$ isoline in yellow and $\langle u \rangle = 0$ isoline in black for all configurations studied.

mid-plane are compared, respectively. The sonic line is shown in yellow and zero streamwise velocity is shown in black. The main features identifiable for the controlled cases are the suction effect, which eliminates a great portion of the recirculation zone (black line) and the perturbation of the incoming TBL due to the vertical injection, promoting the formation of additional weak shock-expansion systems similar to the case of AJVG (Souverein and Debièvre, 2010).

A comparison of mean flow properties is given in Fig. 13. The lower incoming skin friction level illustrated in Fig. 13(a) highlights the aforementioned perturbation of the upstream TBL for all control cases. Local suction accelerates the near-wall flow, which subsequently leads to an increase in skin friction directly upstream of the individual suction slot. Downstream of the suction slot, the skin friction level drops to greater negative values due to the higher reversed flow amplitude. All control configurations lead to a downstream shift of the mean separation location. The largest effect is observed for control case CB. For this case the skin friction evolution downstream of the suction channel exhibits an upstream shift of the mean reattachment position and an overall higher skin friction level in the relaxation zone. The mean wall pressure distribution in Fig. 13(b) clearly shows a reduction of the upstream influence length for control case CB. The interaction lengths L_{int}/δ_0^r are 3.24, 3.26, 2.75 and 3.09 for the cases NC, CA, CB and CC, respectively. The ability of the control mechanism to reduce the amount of mean recirculating flow is evaluated by analysing the bubble mass per unit span enclosed within the zero streamwise velocity iso-line, see Fig. 13(c). Suction applied within the rear part of the separation bubble (CC) reduces the bubble mass by about 63%, possibly being a direct consequence of the higher mass-flow ratio $\dot{m}_{ch}/\dot{m}_{bl}$ for this case (see Table 3 for details).

The influence of each control configuration on turbulence intensity is studied in the following. Fig. 15 shows contours of the

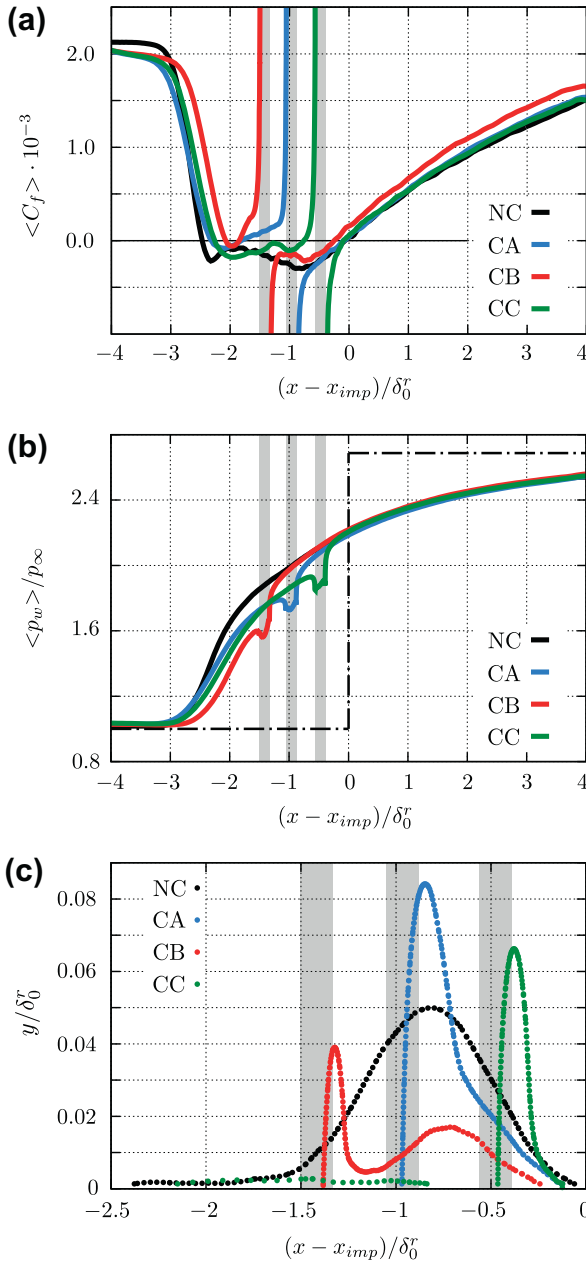


Fig. 13. Mean flow properties in the vicinity of the interaction region. (a) Skin friction (C_f) (b) and wall-pressure (p_w)/ p_∞ evolution in the streamwise direction. (c) Bubble topology represented through zero streamwise velocity isoline $\langle u \rangle = 0$. Grey shaded areas indicate individual suction locations.

Table 3
Mean-flow quantities of all cases studied.

Case	NC	CA	CB	CC	
Interaction length ^a	L_{int}/δ_0^r	3.24	3.26	2.75	3.09
Max. bubble height ^b	h_{max}/δ_0^r	0.050	0.084	0.038	0.066
Massflow ratio ^c	$\dot{m}_{ch}/\dot{m}_{bl}$ (%)	–	2.66	2.05	3.15
Bubble mass ^d	$m/(\rho_\infty \delta_0^{r^2})$	0.036	0.030	0.014	0.013

^a Distance between the mean reflected shock foot position and theoretical inviscid impingement point.

^b Measured through $\langle u \rangle = 0$ iso-line.

^c Massflow ratio between the channel flow \dot{m}_{ch} and the undisturbed TBL \dot{m}_{bl} .

^d Bubble mass per unit span.

resolved Reynolds shear stress, the boundary-layer thickness evolution (white) and the sonic line (black) for all cases. White dotted lines indicate suction and injection locations. For the

baseline configuration a high level of Reynolds shear stress is found along the detached shear layer within the interaction region $-3 < (x - x_{imp})/\delta_0^r < 1$. Its maximum is located approximately one boundary-layer thickness downstream of the mean reattachment location ($(x - x_{imp})/\delta_0^r \approx 1$), confirming the findings by Pirozzoli and Grasso (2006). A high Reynolds shear stress level $\langle u'v' \rangle$ is found along the reflected shock, which is consistent with experimental measurements by Piponniau (2009) and directly associated with the shock motion. Reynolds shear stress changes sign at the tip of the incident shock as a consequence of its flapping motion (Shahab, 2006). For all control cases additional unsteady shocks can be identified in the vicinity of the injection slots (white dotted lines). At the same location, the formation of shear layers due to small recirculation zones directly upstream and downstream of the injection position leads to an increased level of turbulence in this region, which is then convected downstream and interacts with the original reflected shock. The adverse pressure gradient induced by the reflected shock bulges the incoming shear layer, resulting in a spot of increased Reynolds shear stress within the interaction zone. This phenomenon is more pronounced for control cases CA and CC. It is interesting to note that the flapping motion of the incident shock tip and the reflected shock dynamics are significantly reduced for configuration CC, whereas for control case CA the shock-excursion length is increased and for CB comparable to the baseline configuration. Considering the overall boundary-layer thickness evolution (white line in Fig. 15), one can conclude that the present control mechanism has not much effect on the downstream boundary-layer. Amplification factors for Reynolds shear stress and turbulent kinetic energy are reported in Table 4, which represent the ratio of the maximum value of a particular Reynolds stress component after or within the interaction

Table 4
Turbulence amplification factors.

Amplification ^a	NC	CA	CB	CC	DNS ^b
$\langle u'v' \rangle$	3.11	3.11	3.17	2.91	3.2
$0.5\langle u'_i u'_i \rangle$	2.64	2.82	3.19	2.29	2.7

^a Compared to the undisturbed boundary-layer.

^b Pirozzoli and Grasso (2006), Ma = 2.25, $\Theta = 8^\circ$.

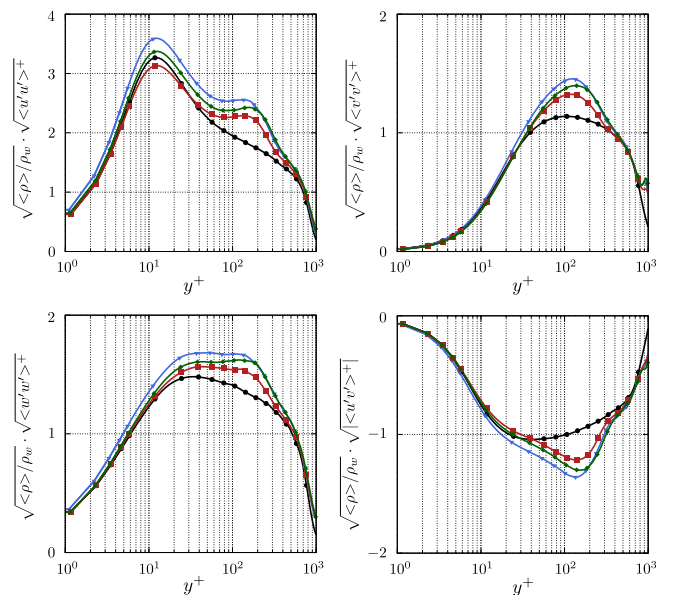


Fig. 14. RMS Reynolds stress profiles with density scaling evaluated at $x^* = (x - x_{imp})/\delta_0^r = -3$ for all cases studied: (●) NC; (▼) CA; (■) CB; (◆) CC.

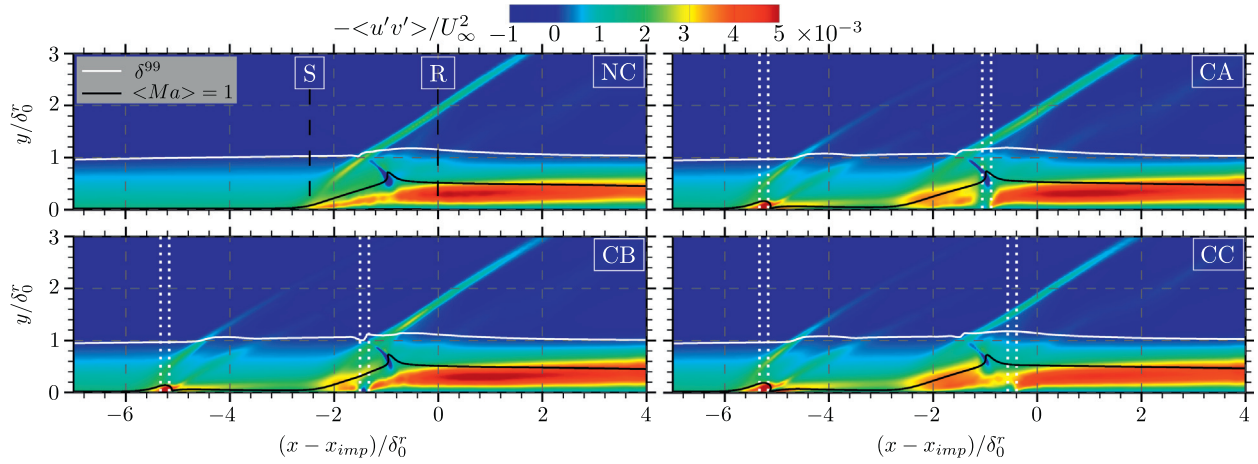


Fig. 15. Mean resolved Reynolds shear stress together with boundary-layer thickness in white and sonic line in black. Vertical dotted lines represent suction and injection locations, respectively. Mean separation and reattachment positions are indicated for the baseline case.

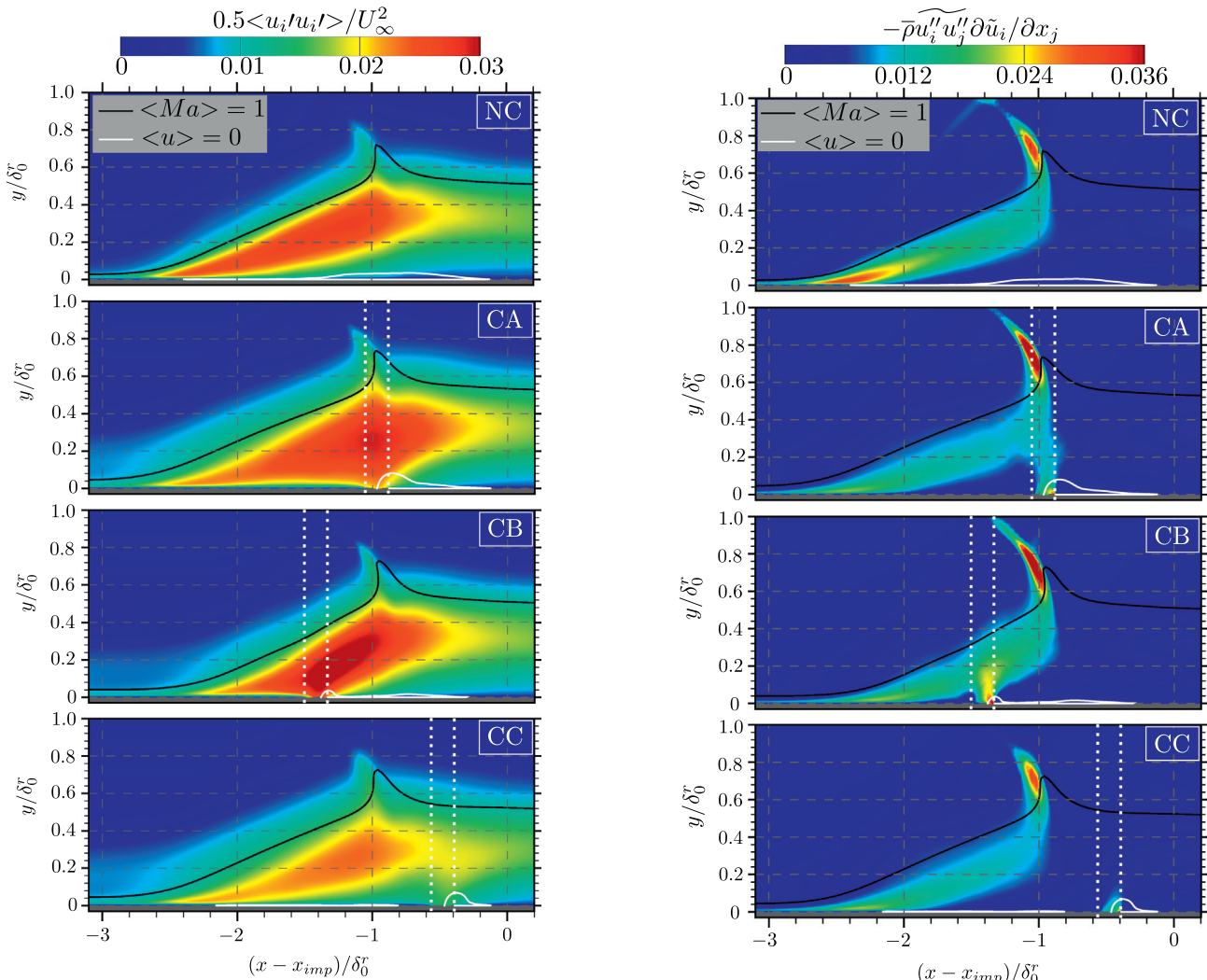


Fig. 16. Resolved turbulent kinetic energy together with zero streamwise velocity iso-line in white and sonic line in black in the vicinity of the interaction zone. Vertical dotted lines represent suction locations.

region to the peak value of the same stress component in the undisturbed incoming turbulent boundary layer. The baseline case is overall in good agreement with the DNS data of Pirozzoli and

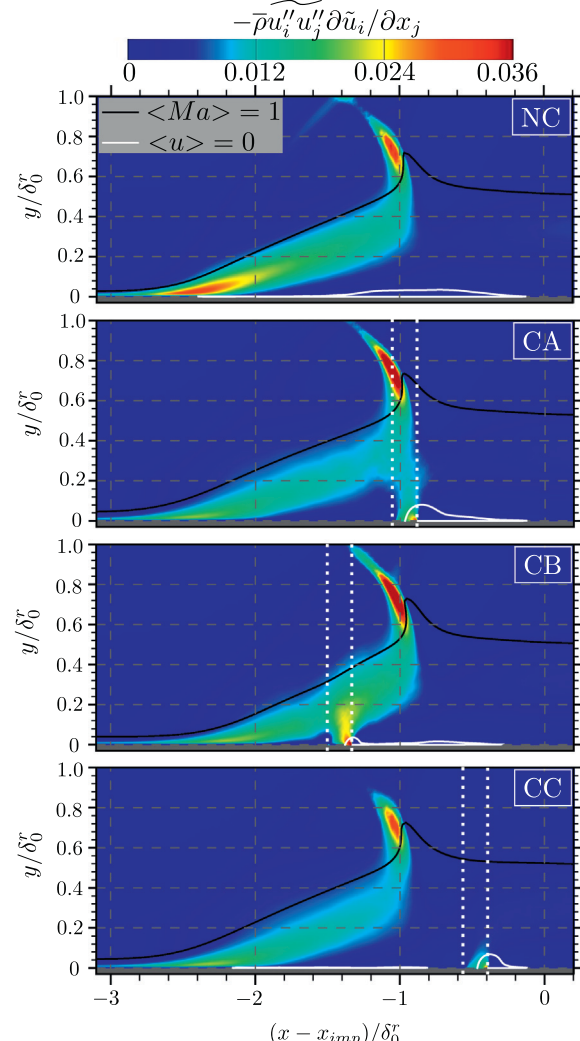


Fig. 17. Resolved turbulence kinetic energy production together with zero streamwise velocity iso-line in white and sonic line in black in the vicinity of the interaction zone. Vertical dotted lines represent suction locations.

Grasso (2006). Reduced amplification for both Reynolds normal and shear stresses is observed if suction is applied in the rear part of the interaction zone, with lowest values for control case CC.

The influence of the cross-jet on turbulence is further addressed in Fig. 14, where we present Reynolds stresses in Morkovin scaling at the streamwise pre-interaction position $(x - x_{imp})/\delta_0^r = -3$. For all control cases the equilibrium turbulence state is not recovered before the reflected shock foot position is reached. While the near-wall turbulence is very similar to the uncontrolled case, increased Reynolds stresses are observed in the logarithmic region around $y^+ \approx 100$ for all control configurations. The higher turbulence level within the range $y^+ \approx 70, \dots, 200$ ($y/\delta_0^r \approx 0.09, \dots, 0.26$) is directly associated with the shear layers that are generated at each discrete suction slot and subsequently convected downstream, see Fig. 15. This implies that it is impossible to differentiate between effects of suction and injection on separation reduction.

A close-up of the interaction zone is shown in Fig. 16, where we present contours of resolved mean TKE, the zero streamwise velocity iso-line in white and the sonic line in black. Without flow control, turbulence is generated when approaching the shock system with TKE maxima being located in the region around the mean separation and along the detached shear layer that originates from it. For all control configurations, the incoming subsonic layer is thicker than for the baseline case. This is a direct consequence of the vertical injection upstream of the SWBLI. However, the zero streamwise velocity iso-line shows that control cases CA and CB significantly reduce the spatial extent of the recirculation zone upstream of the suction slots. Considering the TKE contours, suction applied within the inclined detached shear layer region $(-2.6 < (x - x_{imp})/\delta_0^r < -0.8)$ leads to a strong increase of turbulence, whereas suction applied in the rear part of the bubble (CC) damps turbulent fluctuations. For all three control configurations an increased incoming turbulence level can be observed up to wall distances $y/\delta_0^r \approx 0.3$, which results from additional shear layers directly downstream of the injection slot, see Fig. 15. By investigating contours of turbulence production P , Fig. 17, we find that the deflection of the shear layer towards the suction location strongly enhances turbulence production. This in turn explains the higher TKE level for control cases CA and CB in this region. Considering suction configuration CC, the inclined shear layer remains essentially unaffected and the near-wall flow acceleration contributes to an overall lower turbulence level. As will be seen below, the reflected shock dynamics is significantly weakened for case CC,

which explains the overall lower turbulence level for this configuration.

The influence of the suction location on unsteady reflected shock dynamics is investigated in the following. Fig. 18 illustrates the wall-pressure spectrum for all cases studied. The spectra $f \cdot PSD(f)$ are plotted in a linear scale against $\log(f)$, resulting in an energetic scaling. The area under the resulting curve is proportional to the energy $E_{f_a-f_b}^2$ of the signal between f_a and f_b (Gatski and Bonnet, 2009):

$$E_{f_a-f_b}^2 = \int_{f_a}^{f_b} [f \cdot PSD(f)] d(\log f) = \frac{\langle p' p' \rangle}{(\rho_\infty U_\infty^2)^2}, \quad (12)$$

This scaling guarantees that different configurations and streamwise positions are directly comparable with respect to the frequency and energy content of the wall-pressure signal. From Eq. (12) it is obvious that the resulting contour plot can be interpreted as wall-pressure load. In all spectra we highlight characteristic Strouhal numbers found for the baseline case NC by white horizontal lines. Moreover, black bullets represent the most dominant low-frequencies for each individual configuration. For control cases, suction and injection positions are again illustrated through vertical dashed lines. As already observed in Fig. 15, all control configurations exhibit additional low-frequency content near the injection and suction position. The broadband peak centered around $St \approx 1$ after the suction location indicates that none of the investigated control techniques alters the large-scale turbulence dynamics upstream of the interaction zone significantly. The low-frequency associated to the reflected shock dynamics is still apparent for all three control cases but shifted to higher Strouhal numbers with the greatest effect for configuration CC, see Table 5 for details.

Table 5

Reflected shock characteristic Strouhal numbers.

Case	NC	CA	CB	CC
$St^a = f\delta_0^r/U_\infty$	0.005/0.014	0.01/0.026	0.014/0.033	0.017
$\Delta St/St (\%)$	-/-	100/85	180/135	240/21
n_{LFC}^b	5.6/15.6	9.4/24.6	13.0/30.6	17.1

^a Characteristic Strouhal numbers associated to the black bullets (●) in Fig. 18.

^b Number of low-frequency cycles captured within the available integration time.

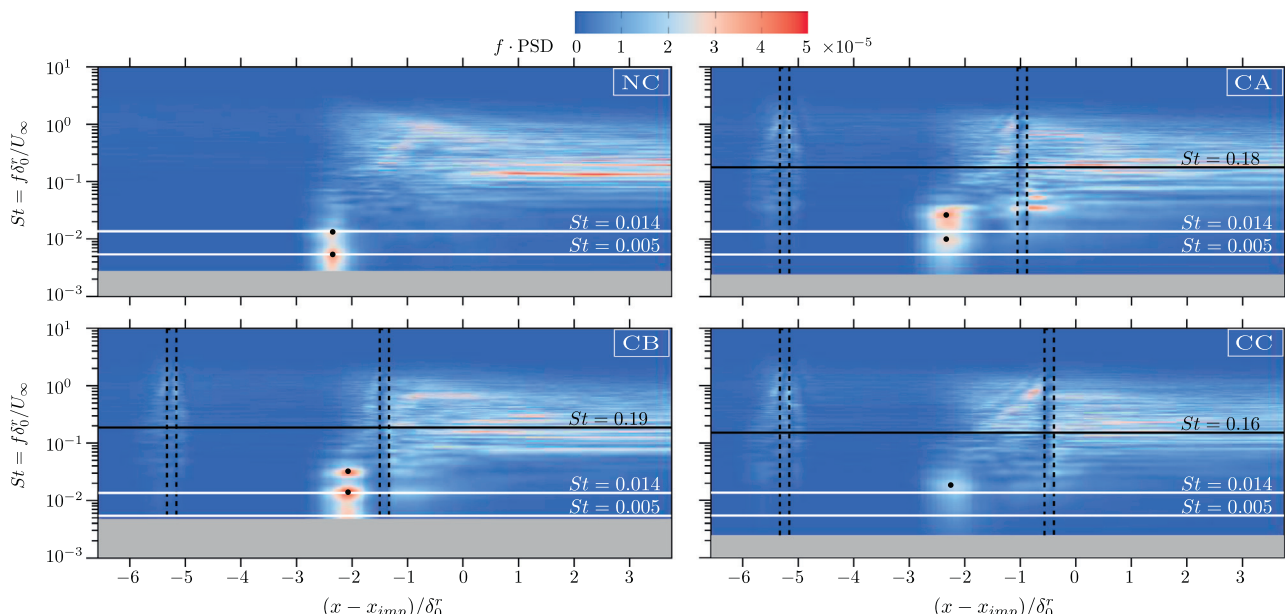


Fig. 18. Weighted power spectral density (PSD) of spanwise-averaged wall-pressure probes for all cases studied. Contour: $f \cdot PSD(f)$.

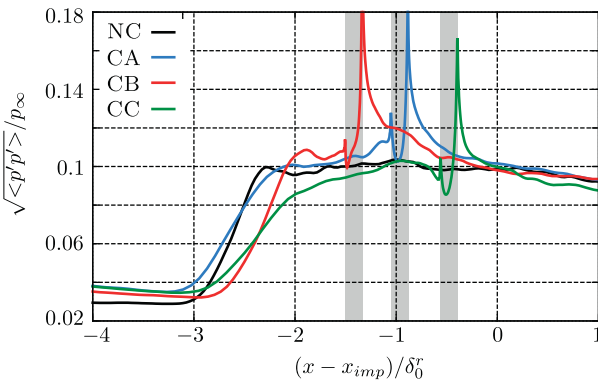


Fig. 19. Root-mean-square profiles of wall-pressure fluctuations in streamwise direction.

One could argue that this is a direct consequence of the lower bubble mass (Souverein and Debièvre, 2010), provided that the pulsation of the recirculation zone is responsible for the low-frequency unsteadiness observed Pirozzoli et al. (2010), Grilli et al. (2012). The acoustic coupling provided by the passive-channel concept explains that the same level of low-frequency content is present in the direct vicinity of the suction and injection positions. However, an acoustic feedback mechanism through the channel, which locks the reflected shock dynamics, can be excluded since the characteristic Strouhal number associated with an acoustic disturbance that travels through the channel (see horizontal black lines in Fig. 18) is approximately one order of magnitude larger than the one observed for the reflected shock. As characteristic velocity for the feedback Strouhal number we use the superposition of the average convective velocity and the average speed of sound within each individual channel. The contour in Fig. 18 further reveals an overall lower energy level for control case CC in the low-frequency regime.

Integrating the wall-pressure spectra at each streamwise location results in the RMS of wall-pressure fluctuations $\sqrt{\langle p'p' \rangle / p_\infty}$ shown in Fig. 19. Large amplifications of pressure fluctuations are found around the reflected shock foot, while secondary peaks can be observed at the discrete suction locations. Besides the change in interaction length L_{int} as already discussed in conjunction with the wall-pressure evolution, Fig. 13, one can further observe a significantly lower amplification level for control configuration CC near the reflected shock foot and after the SWBLI, consistent with previous discussions related to Figs. 15 and 17.

5. Conclusions

We have studied a passive flow-control mechanism for the interaction of an oblique shock with a turbulent flat-plate boundary-layer using well resolved large-eddy simulation. The shock is generated by a 8.8° wedge at a freestream Mach number of $M_{\infty} = 2.3$. The Reynolds number based on the incoming boundary-layer thickness is $Re_{\delta_0} = 60.5 \times 10^3$.

We found that suction applied within the separation zone significantly alters turbulence evolution in this region. Suction acting within the region of the inclined detached shear layer (CA and CB) strongly increases the turbulence level through a deflection towards the discrete suction slot, whereas suction applied in the rear part of the separation bubble (CC) lowers the overall turbulence level. Of course not only the shear layer contributes to turbulence production, but also the unsteady motion of the reflected shock. By investigating contours of resolved Reynolds shear stress we found that control configuration CC significantly reduces the reflected shock dynamics and the flapping motion associated with

the incident shock tip. Both findings support the observation of reduced turbulence levels for this case compared to the baseline configuration without control (NC).

The influence of the control method on the low-frequency unsteadiness has been addressed through a Fourier analysis of wall-pressure probes. All configurations shift the high-energy content associated with the reflected shock to higher frequencies, possibly as a direct consequence of the reduction in bubble mass. Configurations CB and CC are most efficient and at the same time show the largest reduction in bubble mass. Weighted power spectral densities in energetic scaling reveal a remarkably reduced low-frequency energy level for case CC. The streamwise evolution of wall pressure fluctuations shows a significant reduction of wall pressure loads for control case CC around the mean reflected shock foot, which is a direct consequence of the mitigated reflected shock dynamics.

For weak interactions, such as the investigated configurations, the control efficiency strongly depends on the suction position. For stronger shocks with larger deflection angles and otherwise identical flow conditions, the wall-pressure distribution within the recirculation region exhibits a significant pressure plateau due to the presence of a larger separated zone. Consequently, the control method becomes less sensitive with respect to suction position. Moreover, control acts on a higher pressure jump so that one may expect an increased effectiveness for strong interactions.

Acknowledgements

Financial support has been provided by the German Research Foundation (DFG) through the SFBTRR 40 project. Computational resources have been provided by the Leibniz-Rechenzentrum München (LRZ). Vito Pasquariello would like to thank Bernd Budich and Jan Matheis for fruitful discussions.

References

- Adams, N.A., 2000. Direct simulation of the turbulent boundary layer along a compression ramp at $M = 3$ and $Re_\theta = 1685$. *J. Fluid Mech.* 420, 47–83. <http://dx.doi.org/10.1017/S0022112000001257>.
- Beresh, S.J., Clemens, N.T., Dolling, D.S., 2002. Relationship between upstream turbulent boundary-layer velocity fluctuations and separation shock unsteadiness. *AIAA J.* 40, 2412–2422. <http://dx.doi.org/10.2514/2.1609>.
- Bisek, N., Rizzetta, D., Poggie, J., 2012. Exploration of plasma control for supersonic turbulent flow over a compression ramp. In: 42nd AIAA Fluid Dynamics Conference and Exhibit, American Institute of Aeronautics and Astronautics, New Orleans, Louisiana, doi: 10.2514/6.2012-2700.
- Blinde, P.L., 2008. Effects of Micro-Ramps on a Shock Wave/Turbulent Boundary Layer Interaction. Master thesis. Delft University of Technology.
- Délery, J., 1985. Shock wave/turbulent boundary layer interaction and its control. *Progr. Aerosp. Sci.* 22, 209–280. [http://dx.doi.org/10.1016/0376-0421\(85\)90001-6](http://dx.doi.org/10.1016/0376-0421(85)90001-6).
- Délery, J., Dussauge, J.P., 2009. Some physical aspects of shock wave/boundary layer interactions. *Shock Waves* 19, 453–468. <http://dx.doi.org/10.1007/s00193-009-0220-z>.
- Doerffer, P., Hirsch, C., Dussauge, J.P., Babinsky, H., Barakos, G.N., 2011. In: Unsteady Effects of Shock Wave Induced Separation. Notes on Numerical Fluid Mechanics and Multidisciplinary Design, vol. 114. Springer, Berlin, Heidelberg. <http://dx.doi.org/10.1007/978-3-642-03004-8>.
- Dolling, D.S., 2001. Fifty years of shock-wave/boundary-layer interaction research: what next? *AIAA J.* 39, 1517–1531. <http://dx.doi.org/10.2514/2.1476>.
- Dolling, D., Bogdonoff, S., 1981. An experimental investigation of the unsteady behavior of blunt-fin-induced shock wave turbulent boundary layer interaction. In: 14th Fluid and Plasma Dynamics Conference, American Institute of Aeronautics and Astronautics, Palo Alto, California, doi: 10.2514/6.1981-1287.
- Dupont, P., Haddad, C., Debièvre, J.F., 2006. Space and time organization in a shock-induced separated boundary layer. *J. Fluid Mech.* 559, 255. <http://dx.doi.org/10.1017/S0022112006000267>.
- Dussauge, J.P., Dupont, P., Debièvre, J.F., 2006. Unsteadiness in shock wave boundary layer interactions with separation. *Aerosp. Sci. Technol.* 10, 85–91. <http://dx.doi.org/10.1016/j.ast.2005.09.006>.
- Fulker, J., 1999. The Euroshock programme (A European programme on active and passive control of shock waves), in: 17th Applied Aerodynamics Conference, American Institute of Aeronautics and Astronautics, Norfolk, Virginia, doi: 10.2514/6.1999-3174.

- Ganapathisubramani, B., Clemens, N.T., Dolling, D.S., 2007. Effects of upstream boundary layer on the unsteadiness of shock-induced separation. *J. Fluid Mech.* 585, 369–394. <http://dx.doi.org/10.1017/S0022112007006799>.
- Gatski, T.B., Bonnet, J.P., 2009. Compressibility. *Turbulence and High Speed Flow*. Elsevier, Oxford.
- Ghosh, S., 2010. An Immersed Boundary Method for Simulating the Effects of Control Devices used in Mitigating Shock/Boundary-Layer Interactions. Ph.D. thesis. North Carolina State University.
- Grilli, M., Schmid, P.J., Hickel, S., Adams, N.A., 2012. Analysis of unsteady behaviour in shockwave-turbulent boundary layer interaction. *J. Fluid Mech.* 700, 16–28. <http://dx.doi.org/10.1017/jfm.2012.37>.
- Grilli, M., Hickel, S., Adams, N.A., 2013. Large-eddy simulation of a supersonic turbulent boundary layer over a compression-expansion ramp. *Int. J. Heat Fluid Flow* 42, 79–93. <http://dx.doi.org/10.1016/j.ijheatfluidflow.2012.12.006>.
- Guarini, S.E., Moser, R.D., Shariff, K., Wray, A., 2000. Direct numerical simulation of a supersonic turbulent boundary layer at Mach 2.5. *J. Fluid Mech.* 414, 1–33. <http://dx.doi.org/10.1017/S0022112000008466>.
- Hickel, S., Larsson, J., 2009. On implicit turbulence modeling for LES of compressible flows. In: Eckhardt, B. (Ed.), *Advances in Turbulence XII*. Springer, Berlin Heidelberg, pp. 873–875. http://dx.doi.org/10.1007/978-3-642-03085-7_209.
- Hickel, S., Adams, N.A., Domaradzki, J.A., 2006. An adaptive local deconvolution method for implicit LES. *J. Comput. Phys.* 213, 413–436. <http://dx.doi.org/10.1016/j.jcp.2005.08.017>.
- Hopkins, E.J., Inouye, M., 1971. An evaluation of theories for predicting turbulent skin friction and heat transfer on flat plates at supersonic and hypersonic Mach numbers. *AIAA J.* 9, 993–1003.
- Komminaho, J., Skote, M., 2002. Reynolds stress budgets in Couette and boundary layer flows. *Flow Turbul. Combust.* 68, 167–192. <http://dx.doi.org/10.1023/A:1020404706293>.
- Lee, S., 2009. Large Eddy Simulation Of Shock Boundary Layer Interaction Control Using Micro-Vortex Generators. Ph.D. thesis. University of Illinois.
- Loginov, M.S., Adams, N.A., Zheltovodov, A.A., 2006. Large-Eddy Simulation of Shock-Wave/Turbulent-Boundary-Layer Interaction. Ph.D. thesis. Technische Universität München, doi: 10.1017/S0022112006000930.
- Lumley, J.L., 1978. Computational modeling of turbulent flows. *Adv. Appl. Mech.* 18, 123–176.
- Maeder, T., Adams, N.A., Kleiser, L., 2001. Direct simulation of turbulent supersonic boundary layers by an extended temporal approach. *J. Fluid Mech.* 429, 187–216. <http://dx.doi.org/10.1017/S0022112000002718>.
- McCormick, D.C., 1993. Shock/boundary-layer interaction control with vortex generators and passive cavity. *AIAA J.* 31, 91–96. <http://dx.doi.org/10.2514/3.11323>.
- Piponnau, S., 2009. Instationnarités dans les décollements compressibles: cas des couches limites soumises à ondes de choc. Ph.D. thesis. Université de Provence Aix-Marseille I.
- Pirozzoli, S., Bernardini, M., 2011. Turbulence in supersonic boundary layers at moderate Reynolds number. *J. Fluid Mech.* 688, 120–168. <http://dx.doi.org/10.1017/jfm.2011.368>.
- Pirozzoli, S., Grasso, F., 2004. Direct numerical simulations of isotropic compressible turbulence: influence of compressibility on dynamics and structures. *Phys. Fluids* 16, 4386–4407. <http://dx.doi.org/10.1063/1.1804553>.
- Pirozzoli, S., Grasso, F., 2006. Direct numerical simulation of impinging shock wave/turbulent boundary layer interaction at $M = 2.25$. *Phys. Fluids* 18, 065113. <http://dx.doi.org/10.1063/1.2216989>.
- Pirozzoli, S., Larsson, J., Nichols, J.W., Morgan, B.E., Lele, S.K., 2010. Analysis of unsteady effects in shock/boundary layer interactions. In: *Proceedings of the Summer Program 2010*, Center of Turbulence Research, Stanford.
- Pope, S., 2000. *Turbulent Flows*. Cambridge University Press, Cambridge.
- Priebe, S., Martín, M.P., 2012. Low-frequency unsteadiness in shock wave-turbulent boundary layer interaction. *J. Fluid Mech.* 699, 1–49. <http://dx.doi.org/10.1017/jfm.2011.560>.
- Schlatter, P., Örlü, R., 2010. Assessment of direct numerical simulation data of turbulent boundary layers. *J. Fluid Mech.* 659, 116–126. <http://dx.doi.org/10.1017/S0022112010003113>.
- Shahab, M.F., 2006. Numerical Investigation of the Influence of an Impinging Shock Wave And Heat Transfer on a Developing Turbulent Boundary Layer. Ph.D. thesis. École Nationale Supérieure de Mécanique et d'Aérotechnique.
- Shahab, M.F., Lehnsch, G., Gatski, T.B., Comte, P., 2011. Statistical characteristics of an isothermal, supersonic developing boundary layer flow from DNS data. *Flow Turbul. Combust.* 86, 369–397. <http://dx.doi.org/10.1007/s10494-011-9329-0>.
- Simens, M.P., Jiménez, J., Hoyas, S., Mizuno, Y., 2009. A high-resolution code for turbulent boundary layers. *J. Comput. Phys.* 228, 4218–4231. <http://dx.doi.org/10.1016/j.jcp.2009.02.031>.
- Smits, A.J., Matheson, N., Joubert, P.N., 1983. Low-Reynolds-number turbulent boundary layers in zero and favorable pressure gradients. *J. Ship Res.* 27, 147–157.
- Souverein, L.J., Debièvre, J.F., 2010. Effect of air jet vortex generators on a shock wave boundary layer interaction. *Exp. Fluids* 49, 1053–1064. <http://dx.doi.org/10.1007/s00348-010-0854-8>.
- Touber, E., Sandham, N.D., 2009a. Comparison of three large-eddy simulations of shock-induced turbulent separation bubbles. *Shock Waves* 19, 469–478. <http://dx.doi.org/10.1007/s00193-009-0222-x>.
- Touber, E., Sandham, N.D., 2009b. Large-eddy simulation of low-frequency unsteadiness in a turbulent shock-induced separation bubble. *Theor. Comput. Fluid Dyn.* 23, 79–107. <http://dx.doi.org/10.1007/s00162-009-0103-z>.
- Touber, E., Sandham, N.D., 2011. Low-order stochastic modelling of low-frequency motions in reflected shock-wave/boundary-layer interactions. *J. Fluid Mech.* 671, 417–465. <http://dx.doi.org/10.1017/S0022112010005811>.
- van Driest, E.R., 1956. The problem of aerodynamic heating. *Aeronaut. Eng. Rev.* 15, 26–41.
- Viswanath, P.R., 1988. Shock-wave-turbulent-boundary-layer interaction and its control: a survey of recent developments. *Sadhana* 12, 45–104. <http://dx.doi.org/10.1007/BF02745660>.
- Wu, M., Martín, M.P., 2007. Analysis of shock motion in shockwave and turbulent boundary layer interaction using direct numerical simulation data. *J. Fluid Mech.* 594, 71–83. <http://dx.doi.org/10.1017/S0022112007009044>.